Chemical Engineering Journal 497 (2024) 154648

Contents lists available at ScienceDirect

Chemical Engineering Journal

journal homepage: www.elsevier.com/locate/cej

Heterometallic organic cages as cascade antioxidant nanozymes to alleviate renal ischemia-reperfusion injury

Demei Sun [a,b,1], Yucen Deng [a,b,1], Jiayong Dong [c], Xinyuan Zhu [a], Jinghui Yang [c,*], Youfu Wang [a,*]

[a] School of Chemistry and Chemical Engineering, Shanghai Jiao Tong University, Shanghai 200240, China
[b] School of Pharmacy, China Medical University, Shenyang 110122, China
[c] Department of Organ Transplantation, Shanghai Changzheng Hospital, Naval Medical University, Shanghai 200003, China

ARTICLE INFO

Keywords:
Metal organic cage
Cascade
Nanozyme
Anti-inflammation
Ischemia-reperfusion injury

ABSTRACT

The regulation of reactive oxygen species (ROS) by antioxidant enzymes plays a crucial role in managing tissue ischemia–reperfusion (I/R) injury. However, the imprecise structures of most developed nanozymes pose significant challenges for their structure–activity interpretation and clinical translation. Additionally, the monotonous enzyme-like activity exhibited by most nanozymes also restricts their efficacy. In this study, we have developed well-defined cascade nanozymes based on metal organic cages (MOCs) to effectively eliminate excessive ROS in the context of renal I/R injury. By integrating nickel and cobalt within the MOC, we obtained heterometallic organic cage (HMOC) nanozymes with adjustable metal ratios. The incorporation of these two metals into a single MOC nanozyme not only expands its catalytic activity but also enables it to facilitate complex antioxidant reactions more effectively than traditional multi-step processes. The performance of HMOC cascade nanozymes, which mimic the cascade activities of superoxide dismutase (SOD) and catalase (CAT), in converting superoxide anion radicals ($^{\cdot}O_2^-$) into oxygen and water is synergistically enhanced by the heterometallic interactions within a single metal cluster in the HMOC structure. Through optimization of the metal ratio within HMOC-2, both in vitro and in vivo experiments demonstrate that its ROS-scavenging capacity surpasses that of other groups significantly, thereby effectively alleviating renal I/R injury. This study not only presents well-defined enzyme-like cascade systems but also highlights their promising therapeutic potential for treating renal I/R injury.

1. Introduction

The intricate process of ischemia-reperfusion (I/R), which involves the restoration of blood flow to an organ or tissue that has been deprived of it, can paradoxically have both beneficial and detrimental effects on the body [1–3]. In the case of the kidney, I/R injury is common in kidney transplantation, trauma, or nephrectomy, constituting a significant etiology of acute kidney injury and hampering the long-term recuperation of renal graft function [4–7]. The underlying mechanism responsible for this phenomenon is multifaceted and involves several interconnected pathways, in which the excessive production of intracellular reactive oxygen species (ROS) is the core role and the main cause of subsequent sterile inflammation. ROS is a natural byproduct of mitochondrial metabolism and serve as essential signaling molecules in various cellular processes; however, during I/R injury, mitochondrial respiration is precluded and therefore generates exponential increase of ROS [8,9]. Accordingly, administration of antioxidant would scavenge ROS and limit the progression of reperfusion injury. However, drugs designed to scavenge ROS generated during reperfusion have yet to result in a clinically effective therapy because of the limited efficacy due to their unsustainable one-time exhausted character and poor accumulation at the injured site [10,11]. Therefore, the development of innovative and powerful ROS scavengers to treat renal I/R injury is crucial and pressing [12,13]. To this end, new ROS scavenger drugs with targeted delivery and long-acting properties have sparked significant interest, in which antioxidant nanozymes presents outstanding advantages [14,15].

Nanozymes represent the next generation of artificial enzymes, possessing distinctive physical, chemical, and biological properties

* Corresponding authors.
E-mail addresses: yjh@smmu.edu.cn (J. Yang), wyfown@sjtu.edu.cn (Y. Wang).
[1] These authors contributed equally to this work.

https://doi.org/10.1016/j.cej.2024.154648
Received 4 April 2024; Received in revised form 21 July 2024; Accepted 6 August 2024
Available online 8 August 2024

inherent to nanomaterials along with enzyme-like catalytic activity [16–21]. Nanozymes have garnered significant attention due to their cost-effectiveness, high stability, multifunctionality, and ease of large-scale production in comparison to natural enzymes [22–26]. Antioxidant nanozymes mainly mimic the activity of peroxidase [27,28], superoxide dismutase (SOD) [29], catalase (CAT) [30], etc. Various antioxidant nanozymes with excellent ROS-scavenging performance have been developed to reduce inflammation caused by diverse diseases [31–33]. However, the majority of developed nanozymes exhibit imprecisestructures and face significant challenges in terms of interpreting structure–activity relationships, achieving scalable production, and advancing clinical translation. Moreover, the limited monotonous enzyme activity of these nanozymes also restricts their efficacy. Achieving atomically precise structures and/or multi-enzyme activity in nanozymes represents two urgent objectives in this field [34,35]. Despite some progress being made towards these goals, it remains highly challenging particularly when attempting to integrate both features into a single nanozyme system.

Metal organic cages (MOCs), also known as metal organic polyhedrons (MOPs), are discrete and uniform entities constructed through the coordination of metal ions or clusters with organic components [36–38]. The integration of organic and inorganic properties renders MOCs highly desirable for biomedical applications owing to their precise, stable, cavitied, and adjustable structures, nanoscale dimensions, facile synthesis and modification protocols, as well as excellent biocompatibility.[39,40] Benefiting from their structural characteristics and rich catalytic activity of metal ions or clusters, MOCs serve as promising nanozymes for elucidating the structure–activity relationship and facilitating clinical translation [41,42]. In line with this perspective, octahedral MOCs with same metals within M_4O clusters, MOC-Co and MOC-Ni, were constructed and their antioxidant performance were preliminarily evaluated. The results demonstrated that both MOC-Co and MOC-Ni exhibited SOD-like and CAT-like activities. Notably, MOC-Co displayed stronger SOD-like enzyme activity compared to MOC-Ni, while the latter showed better CAT-like enzyme activity. Considering their individual performances and the cascading nature of SOD and CAT processes (Fig. 1**a**), orchestrating these two active metals into a single MOC nanozyme system holds great promise [43,44]. Firstly, the incorporation of two metals within a single MOC nanozyme broadens its catalytic activities, particularly for the aforementioned cascade antioxidant reaction. Compared to conventional multistep reactions, this cascade nanozyme with dual active sites achieves an elevated level of spatiotemporal opportunities by reducing diffusion barriers, increasing local concentrations of intermediates and improving overall atom economy [45–47]. Secondly, different metals within one M_4O cluster interact synergistically to further enhance the catalytic activities of individual enzyme mimetics [48,49].

To validate the aforementioned hypothesis, we constructed heterometallic organic cages (HMOCs) with adjustable atomic ratios of Co to Ni, denoted as HMOC-1, HMOC-2, and HMOC-3. The catalytic activity of HMOC is significantly higher than that of MOC-Co or MOC-Ni due to the synergistic effect between Co and Ni. Furthermore, by varying the atomic ratio of these two metals, the antioxidant activity of HMOCs can be tailored accordingly. Notably, among them, HMOC-2 exhibits the highest catalytic activities resembling those of SOD and CAT enzymes (Fig. 1**b**). We have also elucidated the underlying mechanism responsible for such enhanced enzyme activity in the HMOC nanozyme system. Moreover, both in vitro and in vivo tests have confirmed its remarkable antioxidant properties. Our findings highlight MOC as a promising candidate for mimetic antioxidant enzymes with potential clinical translation in renal diseases owing to its excellent ROS scavenging ability and anti-inflammatory effects mediated through reduction in immune cell infiltration, suppression of inflammatory cytokine secretion, inhibition of NLRP3 inflammasomes activation as well as alleviation of apoptosis and autophagy (Fig. 1**c**). The precisely defined and stable atomic structures, modifiable cascade enzyme-like activities, and proven biosafety render MOC-based nanozyme a promising candidate for further clinical translation.

2. Materials and methods

2.1. Materials, cells and animals

All chemicals and solvents are commercially available and can be used as received without further purification. Nickel(II) chloride hexahydrate ($NiCl_2{\cdot}6H_2O$), cobalt(II) chloride hexahydrate ($CoCl_2{\cdot}6H_2O$), potassium dihydrogen phosphate (KH_2PO_4), potassium hydrogen phosphate (K_2HPO_4), sodium acetate (NaOAc), sodium hydroxide (NaOH),

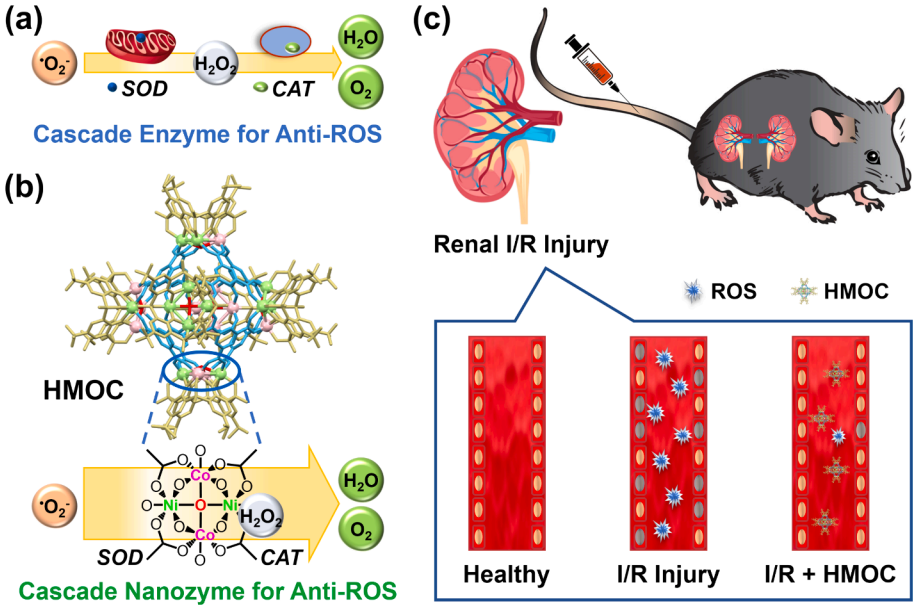

Fig. 1. Schematic illustration of the design of a well-defined heterometallic nanozyme with cascade anti-ROS activity for renal I/R therapy. (a) Cellular cascade enzymes for anti-ROS. (b) Constructing HMOC-based cascade nanozyme for anti-ROS therapy by combinging two metallic catalytic sites into one MOC cluster. (c) The renal I/R injury of mice can be effectively alleviated through treatment with the HMOC cascade nanozyme.

sodium perborate tetrahydrate ($NaBO_3{\cdot}4H_2O$), N,N-dimethylformamide (DMF), methanol (MeOH), glacial acetic acid (HAc), and dimethylsulfoxide (DMSO) were purchased from Shanghai Titan Scientific Co., ltd. (China). Benzene-1,3,5-tricarboxylic acid (H_3BTC), L-methionine (Met), nitrotetrazolium blue chloride (NBT), (−)-riboflavin, ethylenediaminetetraacetic acid disodium salt (EDTA-Na_2), *p-tert*-butylphenol, and tetraethylene glycol dimethyl ether were purchased from Bide Pharmatech Co., ltd. (China). Chloroform ($CHCl_3$), diethyl ether, toluene, H_2O_2, sulfur (S), H_2SO_4, HCl, and HNO_3 were purchased from Sinopharm Chemical Reagent Co., ltd. (China). 4-*tert*-Butylsulfonylcalix [4]arene (SC4A) was synthesized according to previous reports. Total SOD activity assay kit (S0101S), MTT cell proliferation and cytotoxicity assay kit (C0009S), reactive oxygen species detection kit (S0033S), and all materials of western blot (WB) were purchased from Beyotime Biotech. Inc. Chloral hydrate, saline, paraformaldehyde, and cephaloquinoxime for animal use were purchased from Beyotime Biotech. Inc. HK-2 (human kidney 2) cells, fetal bovine serum (FBS), and dulbecco's modified eagle medium (DMEM) were purchased from Beyotime Biotech. Inc. HK-2 cells were grown in DMEM supplemented with 10 % fetal bovine serum and 1 % penicillin–streptomycin in high glucose. The double-distilled water (DDW) was used in the preparation of aqueous solutions (18.25 MΩ).

C57BL/6 mice (female, age of 7–8 weeks, weight 24–26 g) were obtained from Shanghai Laboratory Animal Center (China). All animal experiments were performed in accordance with the guidelines of the National Institute of Health for the Care and Use of Laboratory Animals and approved by the Scientific Investigation Board of Shanghai Jiao Tong University (No. 202301264).

2.2. Instruments

Powder X-ray diffraction (PXRD) spectra were measured on a D8 ADVANCE Da vinci diffractometer using cu Kα radiation. Morphology images and energy spectrum analysis were recorded on an apreo 2S field emission scanning electron microscope (SEM) at 15 kV acceleration voltage. Mass spectrum was measured on a bruker autoflex speed TOF/TOF matrix-assisted laser desorption/ionization time of flight (MALDI-TOF) mass spectrometry with 26,000 resolutions. X-ray photoelectron spectroscopy (XPS) was analyzed using an ESXCALAB Xi+ instrument from thermo Scientific and the C1s peak at 284.8 eV. The amounts of Co and Ni were collected on an inductively coupled plasma optical emission spectrometer (ICP-OES) (Avio 500, PerkinElmer). UV–vis spectra were recorded on a UV-2600i (Shimadzu). Flourier transform infrared spectroscopy (FT-IR) was performed on a Nicolet iS50 using an attenuated total refraction (ATR) attachment. The particle size and zeta potential were detected by particle size and zeta potential analyzer (Malvern ZS90). The change of free radicals was assessed using electron paramagnetic resonance (EPR) spectroscopy (Bruker EMXplus). MTT tests were measured on a microplate reader (BioTek Synergy H4). ROS detection was performed on a flow cytometric analyzer (LSR Fortessa) and fluorescence microscope. Inductively coupled plasma mass spectrometry (ICP-MS) (i CAP Q, Thermo) were used to detect cellular uptake and tissue distribution. Gel photos were obtained on Imager (Agilent). Oxygen content was measured by a portable dissolved oxygen detector.

2.3. Preparation of MOCs

A vial containing $MCl_2{\cdot}6H_2O$ (M = Ni or Co, 0.050 mmol), SC4A (0.010 mmol), H_3BTC (0.030 mmol), DMF (1.0 mL), and methanol (20 μL) was sealed and heated at 100 °C for 24 h. After cooling down, cubic crystals can be observed in the bottom and subsequently separated through centrifugation, wash, and dry under vacuum, donated as MOC-Co and MOC-Ni. HMOCs can be prepared following the above procession, where the input amounts of $CoCl_2{\cdot}6H_2O$ and $NiCl_2{\cdot}6H_2O$ are 0.010 and 0.040 mmol, 0.025 and 0.025 mmol, 0.040 and 0.010 mmol, respectively, donating as HMOC-1, HMOC-2, and HMOC-3, respectively.

2.4. Evaluation of enzyme-like activity

The SOD activities were measured by inhibiting NBT reduction with MOCs in the presence of UV light. The higher the SOD activity, the lower the amount of the reduction product (blue methylhydrazone) and the lower absorbance at 560 nm. Hence, decreased absorbance at 560 nm confirms an increased SOD activity. Under a constant intensity UV lamp, NBT (0.75 mM, 0.25 mL), Met (130 mM, 0.25 mL), EDTA-Na_2 (0.1 mM, 0.25 mL), H_2O (0.20 mL), MOCs (2 mg/mL, 0.05 mL), riboflavin (0.02 mM, 0.25 mL), and phosphate buffer (pH = 7.4, 50 mM, 1.75 mL) were incubated together, and the changes in absorbance value at 560 nm were measured at intervals. The SOD catalytic abilities between different MOCs were compared, HMOC-2 was still the mimic enzyme with the highest catalytic activity. Therefore, HMOC-2 was selected to conduct subsequent biological experiments. Due to the limited water solubility of NBT, we performed testing using a WST-8-based kit with enhanced aqueous solubility. The superoxide anion radical ($^{\bullet}O_2^-$) reacts with WST-8 to produce a water-soluble formazan dye with maximum absorbance at 450 nm. The reaction step is susceptible to inhibition by SOD, and thus the activity of SOD shows an inverse relationship with the quantity of formazan dye produced. We evaluated the inhibitory effect of five MOCs (MOC-Co, MOC-Ni, HMOC-1, HMOC-2, and HMOC-3) on $^{\bullet}O_2^-$, at various concentrations (7.8, 15.6, 31.25, 62.5, 125, 250 μg/mL). To further elucidate the SOD-like activity of MOCs, we utilized EPR for a more intuitive evaluation. 5,5-dimethyl-1-Beroxo-n-oxide (DMPO) serves as an effective free radical trapping agent, capable of forming spin adducts upon reacting with $^{\bullet}O_2^-$. The resulting spin adducts can be detected by EPR spectroscopy, offering a direct reflection of the $^{\bullet}O_2^-$ content in the reaction system. Met (130 mM, 0.25 mL), EDTA-Na_2 (0.1 mM, 0.25 mL), H_2O (0.20 mL), MOCs (2 mg/mL, 0.05 mL), riboflavin (0.02 mM, 0.25 mL), DMPO (100 mM, 70 μL) and phosphate buffer (pH = 7.4, 50 mM, 1.68 mL) were thoroughly mixed together and then placed in a nuclear magnetic resonance tube within a capillary for subsequent UV irradiation at both time points of 0 s and 20 s before measuring the EPR spectra. The CAT-like activity assays of MOCs were carried out at room temperature by measuring the generated oxygen using a handy oxygen detector. In a typical test, 60 μL of 30 % H_2O_2 solution was added to 14.94 mL of buffer solution (pH = 7.2), and then 10 μL of MOCs (2 mg/mL in DMSO) was added. The generated oxygen solubility (unit: mg/L) was recorded from 0 to 6 min. The kinetic assay of the catalytic decomposition of H_2O_2 by MOC (MOC-Co + MOC-Ni or HMOC-2) (13 μg/mL) was performed by adding different amounts (0, 15, 30, 45, 60, 75 μL) of 30 % H_2O_2 solution into buffer solution with a final volume of 15 mL.

2.5. DFT simulations

All geometric structures, including local minima and transition states (TS), were fully optimized using B3LYP density functional and 6-31G (d, p) basis set. In order to identify whether the stagnation point is a local minimum or a transition state, and to obtain the Gibbs free energy, harmonic frequency analysis was performed on each structure. In our calculations, the PCM solvation model is used to simulate water environments. All calculations were performed using the Gaussian 09 software package (Gaussian, Wallingford CT, USA, 2009).

2.6. Hemolysis assay

The whole blood of healthy mice was collected in a 2 mL EP tube, and the blood was centrifuged at 2000 rpm for 5 min to remove the upper serum and obtain erythrocytes. Then erythrocytes were washed three times with PBS, and 0.5 mL erythrocytes were diluted with 10 mL PBS. Then 0.5 mL of MOCs solution in PBS (800 μg/ mL), PBS, or DDW were added to 0.5 mL erythrocytes suspension, respectively. All sample tubes

were kept at room temperature for 2 h and then centrifuged at 2000 rpm for 5 min. Finally, the experimental result was recorded by a camera.

2.7. Cytotoxicity assay

To assess the cytotoxic effect of MOCs, a commercial kit was used to detect the viability of HK-2 cells. HK-2 (7000 cells/well) cells were added into a 96 well plate, and cultured at 37 °C for 12 h. Different concentrations (0, 25, 50, 100, 200, 400, 800 μg/mL, 10 μL) of MOCs solution in PBS were added in cells and cultured for another 24 h. Afterwards, the cells were gently washed by PBS (pH 7.4) for three times. The thiazolyl blue tetrazolium bromide (MTT) solution (100 μL) was added to each well individually and incubated for 4 h in the dark. Subsequently, the cell supernatant was collected using a micropipettor, followed by addition of 150 μL of DMSO. After thorough agitation for 10 min to completely dissolve MTT crystals, cell viability was assessed using a microplate reader at absorbance wavelengths of 570 nm.

2.8. Cellular internalization of HMOC-2

For in-vitro cellular uptake assays, HK-2 cells were inoculated into 10 mm tissue plates at the density of 10,000 cells/mL for 24 h. HMOC-2 (final concentration 20 μg/mL) was added to each plate and cultured for 2 h, 4 h, 8 h or 12 h, respectively.

For in-vitro cellular retention assays, HK-2 cells were inoculated into 10 mm tissue plates at the density of 10,000 cells/mL for 24 h. HMOC-2 (final concentration 20 μg/mL) was added to each plate and cultured for 12 h. Then, the medium was extracted and fresh medium was added. Subsequently, the cells were collected at 4 h (12 + 4h) and 8 h (12 + 8h) respectively.

We used ICP-MS to quantify the cellular uptake of HMOC-2. Then the cells were trysinized with trysin, and collected by centrifugation, washed with PBS buffer for 3 times. For traditional ICP-MS analysis, the samples were digested in a solution containing 0.25 mL HNO_3 (68 %) and 0.75 mL HCl (38 %) for 4 h at 110 °C. After cooling, the samples were diluted with HCl (2 %) to 10 mL. Co and Ni contents were then detected by ICP-MS.

2.9. Evaluation of intracellular ROS-scavenging ability

The intracellular levels of ROS were assessed using the fluorescent probe 2′,7′-dichlorodihydrofluorescein diacetate (DCFH-DA), which reacts with intracellular free radicals to produce dichlorofluorescein (DCF), a fluorescent product. The HK-2 cells were cultured in 6-well microplates (7000 cells/well) at 37 °C for 12 h. After replacing the culture medium, the experimental group was treated with HMOC-2 (final concentration 20 μg/mL) and further incubated at 37 °C for an additional 6 h. Hydrogen peroxide (500 mM) or $Na_2S_2O_4$ (2 mM) were added to each well for another 4 h. Subsequently, cells were harvested and subjected to labeling with the fluorescent probe DCFH-DA according to the flow cytometry analysis manual (BD Biosciences, franklin Lakes, NJ, USA).

2.10. Induction of renal I/R model

Mice were anesthetized with sodium pentobarbital (50 mg/kg, intraperitoneally). After a right flank incision, the right renal pedicle was clamped for 30 min with a nontraumatic microaneurysm clamp (Shanghai medical Instruments, Shanghai, China). The left contralateral kidney was considered as sham surgery. The incision was temporarily closed during ischemia. Upon removal of the microaneurysm clamps, the flank was closed after visual verification of reperfusion. Body temperature was maintained using an adjustable heating pad. All mice received intraperitoneal injection of 0.5 mL isotonic saline post-surgery and were sacrificed at specified reperfusion time points. HMOC-2 (250 μg/mL, 200 μL) injection was injected through the tail vein.

2.11. Pharmacokinetics analysis

The mice were sacrificed at the designated time points. Blood and all organs were collected, weighted and digested in a solution containing 0.25 mL HNO_3 (68 %) and 0.75 mL HCl (38 %) for 12 h at 110 °C. After cooling, the samples were diluted with HCl (2 %) to 10 mL. Co and Ni contents were then detected by ICP-MS.

2.12. Serum biochemistry analysis

The mice were sacrificed at the designated time points. All serum samples were collected and subjected to centrifugation at 5000 rpm for 10 min. ALP, ALT, AST, CRE, LDH, and BUN levels were quantified using an automated analyzer (Cobas 8000, Roche, Germany) equipped with the c702 module.

2.13. Histopathological evaluation

The mice were sacrificed at the indicated time points. The mouse kidneys were cut coronally, fixed in 10 % buffered formalin, embedded in paraffin, and sectioned at a thickness of 3 μm. The sections were stained with hematoxylin and eosin to assess histological injury. Kidney sections were labeled blindly and randomly observed by two investigators. A semiquantitative pathological assessment on a scale of 0–4 was performed to grade the degree of renal tubular injury: 0 = no identifiable injury; 1 = necrosis of individual cells; 2 = necrosis of all cells in adjacent proximal convoluted tubules, with the survival of surrounding tubules; 3 = necrosis confined to the distal third of the proximal convoluted tubules, with a band of necrosis extending across the inner cortex; and 4 = necrosis affecting all three segments of the proximal convoluted tubule.

2.14. Immunofluorescence assay

The paraffin and frozen sections of kidneys were processed following a standardized protocol. Subsequently, the sections were incubated overnight with primary antibodies against NGAL, KIM-1, DHE, CD68, MPO, and LC3 obtained from Abclonal (Wuhan, China). Following this step, the slides underwent three washes with PBS and were then incubated with secondary antibodies at room temperature for 1 h. Nuclei staining was performed using DAPI. Finally, the slides were examined and imaged under a fluorescent microscope (Nikon 80i, Tochigi, Japan).

2.15. Real-time PCR analysis

The total renal RNA was extracted using TRIzol reagent (Invitrogen, Shanghai, China) according to the manufacturer's instructions. cDNA was transcribed using a superscript III reverse transcriptase kit (Invitrogen) and oligo d(T) (Applied Biosystems, Waltham, MA, USA). Quantitative RT-PCR analysis was performed with a SYBR RT-PCR kit (Takara, Tokyo, Japan) and the StepOne Real-Time PCR system (Applied Biosystems). All reactions were conducted in a 20 μL reaction volume in triplicate. The relative expression levels for a target gene were normalized against GAPDH. Primers used for RT-PCR analysis are as follows: TNF-α (5′-*AAG CCT GTA GCC CAC GTC GTA-3′, 5′-GGC ACC ACT AGT TGG TTG TCT TTG*-3′), IL-2 (5′-*CCATGA TGC TCA CGT TTA AAT TTT-3′, 5′-CAT TTT CCAGGC ACT GGA GATG*-3′), IL-6 (5′-*ACA ACC ACG GCCTTC CCT ACT T-3′, 5′-CACGAT TTC CCA GAG AAC ATGTG*-3′), IL-10 (5′-*GCT TTA CTG ACT GGC ATG AG-3′, 5′-CGC AGC TCT AGG AGC ATG TG*-3′), and GAPDH (5′-*TGA CCA CAG TCC ATG CCA TC-3′, 5′-GAC GGA CAC ATT GGG GGT AG*-3′).

2.16. Immunohistochemistry analysis

The paraffin renal sections were handled according to a standard protocol. Briefly, anti-IL-1β, anti-caspase-1, anti-NEK-7, and anti-NLRP3

antibodies (Abclonal) were used to detect protein expression in the kidney tissue. The slides were stained with diaminobenzidine tetrahydrochloride, counterstained with hematoxylin and mounted for microscopic examination.

2.17. Western blotting

Tissues were rinsed with PBS twice and lysed in ice-cold RIPA buffer (Roche, Basel, Switzerland) containing phosphatase and protease inhibitors. Sample proteins were then subjected to 12 % or 15 % sodium dodecyl sulfate–polyacrylamide gel electrophoresis and transferred to nitrocellulose membranes. Membranes were probed with NLRP3, procaspase-1, mature IL-1β, caspase-3, Bax, and Bcl-2 antibodies from Beyotime Biotech. The relative quantity of proteins was determined by a densitometer software (ImageJ, NIH, NY, USA).

2.18. Transmission electron microscopy

The kidneys were perfused and fixed with 2.5 % glutaraldehyde in 0.1 mol/L of PBS solution. Subsequently, the samples were sectioned

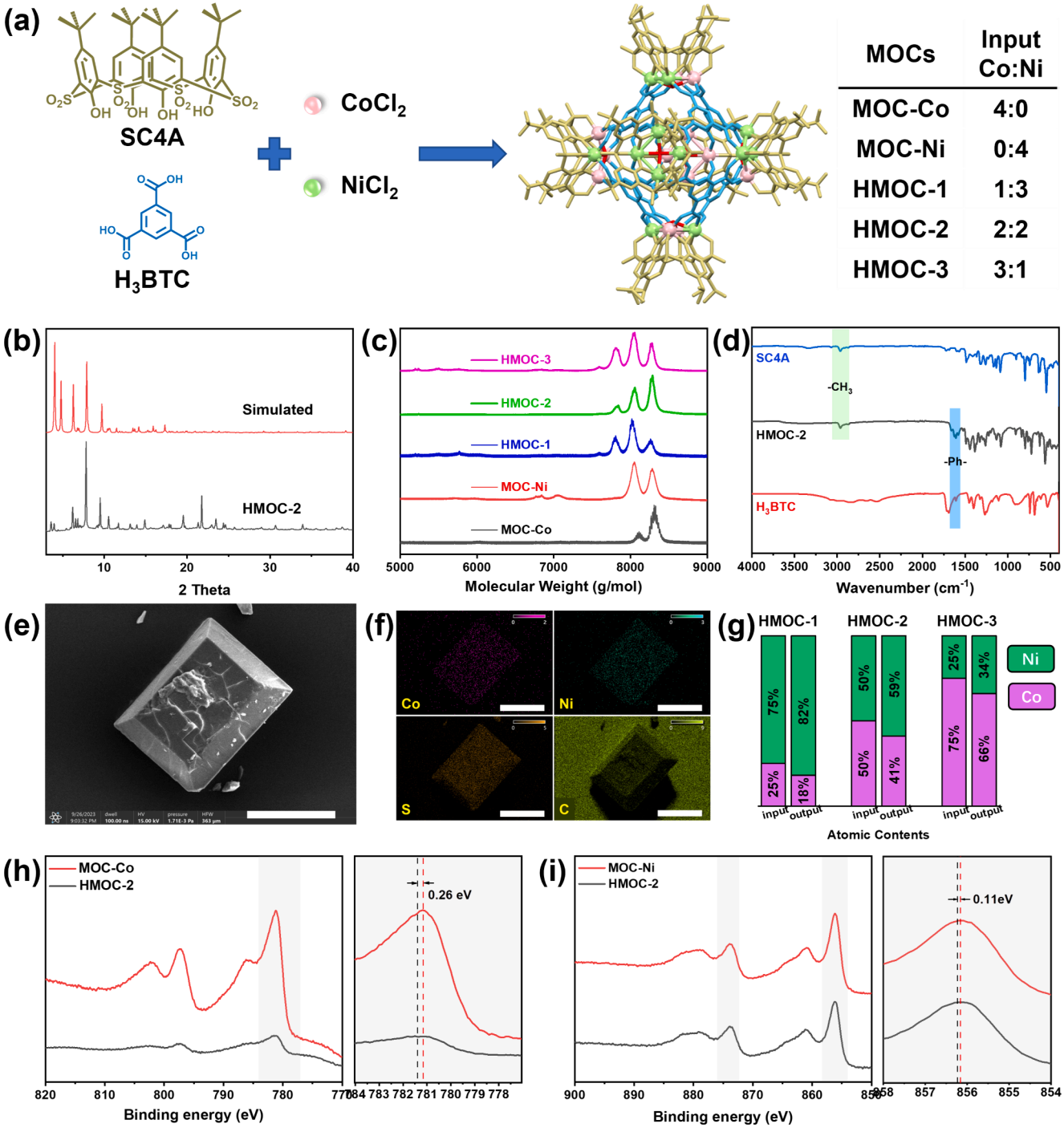

Fig. 2. The synthetic route and structural characterizations of MOCs. (a) The synthesis of MOCs. (b) The powder XRD plot of HMOC-2 and the simulated XRD plot. (c) The MALDI-TOF mass spectra of MOCs. (d) The FT-IR spectra of SC4A, H_3BTC and HMOC-2. (e-f) The SEM image and elemental mapping of crystal HMOC-2. (g) The input and output of two metals in HMOCs. (h-i) The XPS curves of MOC-Co, MOC-Ni and HMOC-2. Scale bars represent 100 μm.

and imaged using a transmission electron microscope (HITACHI H-800, Tokyo, Japan) operating at an acceleration voltage of 80 kV. Autophagy was quantified by assessing the number of double-membrane autophagosome vacuoles per 100 μm cytoplasm.

3. Results and discussion

3.1. Structural characterizations of MOCs

A series of crystal MOCs (MOC-Co, MOC-Ni, HMOC-1, HMOC-2 and HMOC-3) with different metals or metal ratios were obtained through the solvothermal method at 100 °C using 4-*tert*-butylsulfonylcalix[4]arene (SC4A), 1,3,5-benzenetricarboxylic acid (H_3BTC), and hydrated metal chloride ($CoCl_2{\cdot}6H_2O$ and $NiCl_2{\cdot}6H_2O$) similar with previous reports (Fig. 2**a** and **Figure S1**). The input metal ratios of Co/Ni for HMOC-1, HMOC-2, and HMOC-3 are 1/3, 2/2, and 3/1, respectively. Powder X-ray diffraction (PXRD) was firstly employed to verify the structures of these crystal MOCs. As shown in Fig. 2**b**, the sharp diffraction peaks of HMOC-2 indicate its high degree of crystallinity. Moreover, the characteristic diffraction peaks observed align with the simulated single crystal XRD pattern, confirming the successful preparation of HMOC-2. According to the single crystal structures, these MOCs exhibit octahedral geometry and molecular formula of $[(M_4O)_6(SC4A)_6(BTC)_8]$ (M=Co or Ni) [50,51]. To further verify their structures, the molecular weights of these MOCs were measured through matrix-assisted laser desorption ionization time-of-flight (MALDI-TOF) mass spectrometry (Fig. 2**c** and **Figure S2**). The formula weights of MOC-Co and MOC-Ni can be found in 8307 and 8282 Da, respectively, consisting with the calculated values of 8236 and 8228 Da. The HMOCs also exhibited similar mass peaks around 8280 Da, indicating the formation of the expected cage structure. Due to the close atomic weight of Co and Ni, it is challenging to accurately determine the quantity of nickel or cobalt present in HMOC from mass spectrometry. The emergence of new peaks around 7800 Da may come from the incomplete metal clusters (M_4O) within the HMOCs caused by heterometallic distortion. In comparison with relevant components, all MOCs' Fourier transform infrared (FT-IR) spectra demonstrate both characteristic benzene peak at 1606 cm^{-1} from H_3BTC and characteristic methyl peak at 2963 cm^{-1} from SC4A, confirming the successful integration of these building blocks (Fig. 2**d** and **Figure S3**) [51].

The field emission scanning electron microscopy (SEM) and energy dispersive spectroscopy (EDS) were employed to investigate the micrometer-scale crystals with uniform element distribution of HMOCs (Fig. 2**e-f** and **Figure S4**). Furthermore, the precise determination of Ni and Co contents in HMOCs was achieved using an inductively coupled plasma-mass spectrometry (ICP-MS) (Fig. 2**g**). The resulting metal ratios of Co/Ni within HMOCs were found to be 18/82, 41/59, and 66/34 for HMOC-1, HMOC-2, and HMOC-3, respectively. These measured metal ratios closely align with the input values, indicating that Ni exhibits a stronger propensity towards participating in the construction of this type of HMOC compared to Co. The uniform distribution of metals and adjustable metal ratios demonstrate excellent structural controllability achievable through manipulation of the input metal ratios. To investigate the heterometallic interactions within one M_4O cluster in HMOCs, X-ray photoelectron spectroscopy (XPS) was employed to determine element binding energies. Analysis revealed that HMOC-2 simultaneously contains C, O, S, Co, and Ni (**Figure S5**). Moreover, the changes in binding energy were observed between HMOC-2 and mono-metallic MOCs, indicating a random distribution of Co and Ni within HMOC-2 rather than a simple physical mixture of MOC-Co and MOC-Ni (Fig. 2**h-i**) [52]. All the crystal MOCs can be dissolved in dimethyl sulfoxide and then stably dispersed in buffer solution for at least three days (**Figure S6-7**). According to previous studies, the theoretical size of HMOC is approximately 5.5 nm based on crystallographic data [53]. The hydrodynamic diameters of HMOC-1, HMOC-2, and HMOC-3 from the dynamic light scattering (DLS) plots we measured are almost identical, at around 10.1 nm, 9.9 nm, and 9.2 nm respectively; their respective polydispersity indices (PDIs) are extremely small with values of 0.16, 0.16, and 0.20 (**Figure S8**). Considering solvation factors, the measured sizes of the obtained HMOCs are reasonable. The surface charge of HMOCs was also determined to be weakly negative at approximately −1.2 eV (**Figure S9**). Then, the disparity in the maximum absorption peaks of the UV–vis absorption spectra for these MOC solutions (354 nm for HMOC-2 and 351 nm for MOC-Co, 355 nm for MOC-Ni) also suggests a coexistence of two metal atoms within the HMOC instead of a mere physical blend of the two mono-metallic MOCs (**Figure S10**).

3.2. In vitro SOD-like and CAT-like activities of the MOC cascade nanozyme

After successfully demonstrating the controlled synthesis of MOCs, we investigated their cascade nanozyme performance as SOD-like and CAT-like activities. The SOD-like activities of these MOCs were systematically evaluated using nitrotetrazolium blue chloride (NBT) as a sensitive indicator for $^{\bullet}O_2^-$. NBT is specifically reduced by $^{\bullet}O_2^-$ to produce a blue methylhydrazone with a spectral absorbance at 560 nm. The reduction in spectral absorbance at 560 nm indicates the elimination of $^{\bullet}O_2^-$ through SOD-like nanozyme activity. Under UV lamp irradiation, L-methionine (Met), (−)-riboflavin, and ethylenediaminetetraacetic acid disodium salt ($EDTA\text{-}Na_2$) were incubated in phosphate buffer solution at pH = 7.4 to generate $^{\bullet}O_2^-$. We evaluated one blank group and six nanozyme groups, namely MOC-Co, MOC-Ni, MOC-Co + MOC-Ni, HMOC-1, HMOC-2, and HMOC-3 to observe changes in UV–vis absorbance over time. As shown in Fig. 3**a**, all the MOC groups exhibited significant elimination of $^{\bullet}O_2^-$ (**Figure S11-S16**). The physical mixture of MOC-Co and MOC-Ni showed better performance than individual MOC-Co or MOC-Ni alone. Among HMOCs, HMOC-2 demonstrated the highest SOD-like activity based on its spectral evolution over time. To further confirm the exceptional SOD-like activity of HMOC, we conducted the water-soluble tetrazolium (WST) assay using a commercial kit. The $^{\bullet}O_2^-$ reacts with WST to produce a water-soluble formazan dye with maximum absorbance at 450 nm, and SOD effectively inhibits this process. The evaluation of SOD-like nanozyme activity was carried out by measuring the absorbance at 450 nm using a microplate reader. HMOC-2 exhibited remarkable $^{\bullet}O_2^-$ inhibition ability (Fig. 3**b**). Additionally, to assess the $^{\bullet}O_2^-$ scavenging capability of different MOC nanozymes, electron paramagnetic resonance (EPR) spectrometry was employed. The typical EPR signals of $^{\bullet}O_2^-$ are manifested as a narrow six-line spectrum. It is important to note that the distinct peak shape (1:1:1 or 1:1:1:1) observed in EPR studies could potentially be attributed to various factors, such as the configuration of instrument parameters or the affinity between the substance and the spin-trapping agents [54,55]. The EPR signals decreased significantly upon addition of MOC, particularly with HMOC-2, indicating efficient scavenging of $^{\bullet}O_2^-$ (Fig. 3**c** and **Figure S17**).

Furthermore, the CAT-like activities of these MOCs were also investigated. The generated oxygen was detected in the presence of hydrogen peroxide (H_2O_2) and various MOCs using an oxygen detector. The time-dependent CAT-like activities of the aforementioned six groups of MOCs were examined. Notably, MOC-Ni exhibited superior CAT-like activity compared to MOC-Co, while a mixture of MOC-Co and MOC-Ni showed enhanced performance compared to mono-metallic MOCs (Fig. 3**d**). Moreover, the HMOCs exhibited much higher activity due to the synergistically heterometallic interaction. Among the HMOCs, those with a more balanced cobalt and nickel content demonstrated greater potential for CAT-like activity owing to increased formation of heterometallic clusters. Furthermore, we also investigated the H_2O_2 concentration-dependent CAT-like activities of blank samples, as well as mixtures containing both MOC-Co and MOC-Ni or HMOC-2. As the H_2O_2 concentration increased from 0 to 50 mM, all tested MOCs exhibited enhanced catalytic activities; however, HMOC-2 demonstrated superior performance (**Figure S18-20**).

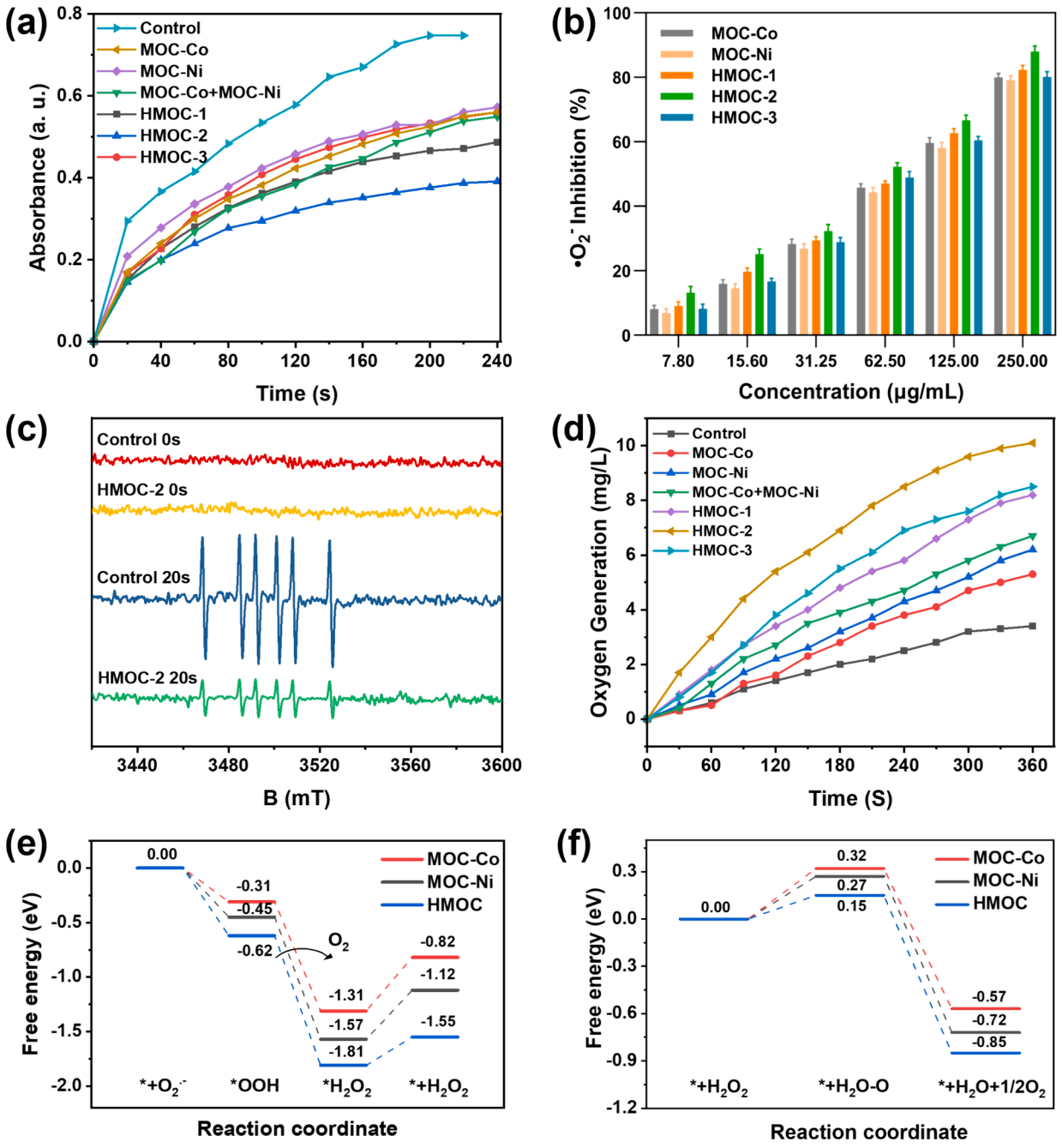

Fig. 3. The antioxidant performance of MOC cascade nanozymes. (a) Typical kinetic curves for monitoring the reduction of NBT in the absence and presence of MOCs. (b) Correlation between the efficiency of $^{\bullet}O_2^-$ elimination and concentrations of MOCs. (c) EPR detection of $^{\bullet}O_2^-$ signals under varying conditions. (d) Typical kinetic curves for monitoring the generation of oxygen in the absence and presence of MOCs. e,f) Gibbs free energy profile for SOD-like and CAT-like reactions. *denotes as adatom.

Due to the exceptional cascade enzyme-like activities exhibited by HMOC, we conducted a theoretical investigation into the underlying mechanisms responsible for the synergistic enhancement of this cascade enzyme-like activity. Considering the metal cluster (M_4O) as the active sites for these enzyme-like processes, six potential structural forms of M_4O clusters can be identified in HMOCs (Figure S21). Three representative structural forms, which reflect the local structure of MOC-Co, MOC-Ni, and HMOC-2, were selected for the calculation of Gibbs free energy in all states (reactant, intermediate, product) during SOD-like and CAT-like catalytic processes using density functional theory (DFT). In the SOD process, the adsorption of $^{\bullet}OOH$ onto the M_4O cluster exhibits a negative change in energy, indicating its spontaneous nature (Fig. 3**e**). Moreover, in comparison to Co_4O and Ni_4O clusters (−0.31 eV and −0.45 eV), the heterometallic Co_2Ni_2O cluster exhibited a reduced adsorption energy of −0.61 eV, indicating its enhanced capability to capture $^{\bullet}OOH$ free radicals. The inclusion of heterometallic clusters can decrease the adsorption energy, enhance reactant concentration on surfaces, and facilitate a rightward shift in the SOD process. Regarding the CAT process, the calculated energy barriers for H_2O_2 adsorption and degradation on M_4O clusters were 0.32 eV, 0.27 eV, and 0.15 eV for Co_4O, Ni_4O, and Co_2Ni_2O clusters respectively (Fig. 3**f**). The reduction in activation energy barrier suggests that less energy is required for heterometallic cluster involvement in the CAT catalytic reaction, thereby significantly promoting H_2O_2 conversion efficiency. The calculated

details and intermediate states during SOD-like and CAT-like processes can be found in supporting information (**Figure S22-23**). These computational findings are consistent with experimental observations demonstrating superior CAT-like activity of MOC-Ni compared to MOC-Co as well as support the notion that HMOCs containing heterometallic clusters exhibit enhanced SOD-like and CAT-like performance relative to mono-metallic MOC-Co or MOC-Ni nanozymes. That is, the presence of approximately equal amounts of Co and Ni is expected to result in a higher proportion of heterometallic clusters statistically within HMOC-2, thereby resulting in its superior catalytic activity [56–58].

3.3. *In vitro ROS-scavenging ability of HMOC-2 to protect HK-2 cells*

We first tested the cytotoxic effects of MOCs and observed little cytotoxicity and hemolytic activity even at a high concentration of 800 μg/ml of MOCs (Fig. 4**a-b**). These MOCs can be effectively uptake (about 25 μg HMOC-2 per million cells) by HK-2 cells through ICP-MS measurements (**Figure S24**). Then the in vitro cytoprotective capacity of MOCs in shielding HK-2 cells from different stressors induced by H_2O_2 treatment or hypoxia/reoxygenation (H/R) exposure has been evaluated. The results of the MTT assay demonstrated that treatment with H_2O_2 or exposure to H/R significantly reduced the viability of HK-2 cells compared to the control group. However, MOCs treatment significantly mitigated this detrimental effect and preserved cell viability, particularly HMOC-2, suggesting its potential as a protective agent against oxidative stress-induced cellular injury (Fig. 4**c-d**).

To further investigate the ROS clearance in HK-2 cells, we employed DCFH-DA, a cell-permeable ROS probe, to detect intracellular ROS of HK-2 cells [59]. When treated with H_2O_2, MOC-Ni or MOC-Co alone failed to effectively scavenge the ROS, whereas the HMOCs exhibited significant efficacy in ameliorating oxidative stress in HK-2 cells, with HMOC-2 demonstrating the highest potency (Fig. 4**e**). Additionally, the ROS scavenging effect of the HMOCs was further confirmed in H/R model. As shown in Fig. 4**f**, the treatment of H/R significantly increased the level of free radicals in HK-2 cells, while MOC-Ni or MOC-Co alone had negligible effects on reducing free radicals. In contrast, HMOC-2 exhibited a remarkable ability to reduce free radical levels in HK-2 cells, indicating excellent ROS clearance capability.

Overall, these findings provide valuable insights into the in vitro antioxidant and renoprotective potential of HMOC-2, highlighting its potential as a therapeutic agent for the prevention or treatment of renal diseases associated with oxidative stress and inflammation.

3.4. *HMOC-2 protected against renal I/R injury*

Considering that HMOC-2 exhibited the most pronounced efficacy in reducing free radical levels among all the tested HMOCs, we have selected HMOC-2 as the primary experimental subject for subsequent in

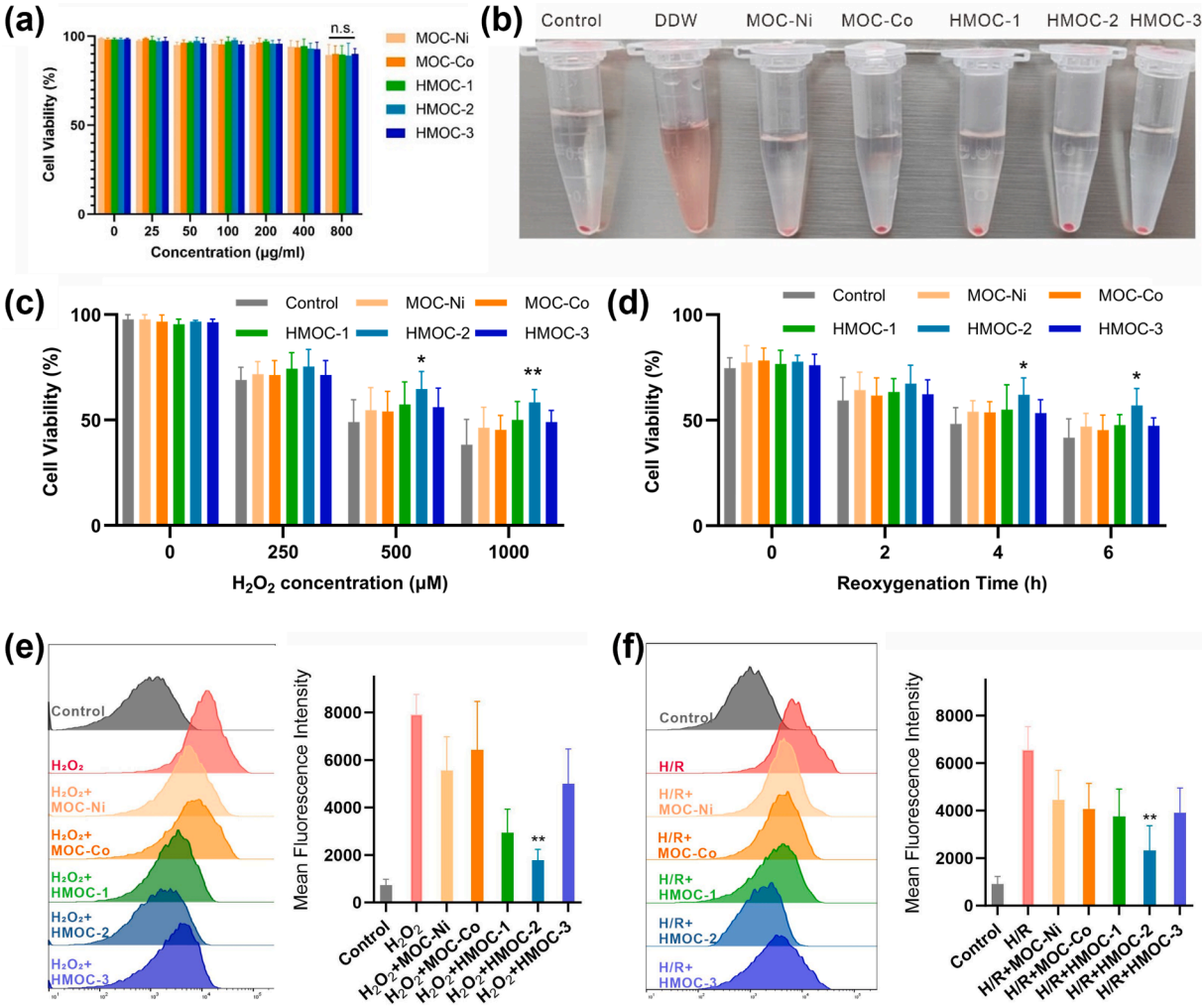

Fig. 4. In vitro cytoprotective and ROS-scavenging ability of MOCs. (a) MTT assay of MOCs on HK-2 cells. (b) Hemolytic assessment conducted with DDW and MOCs on HK-2 cells. (c-d) MTT assay of MOCs on H_2O_2 treated or H/R assaulted HK-2 cells. (e-f) Representative flow cytometry data of HK-2 cells treated with MOCs after stimulation with H_2O_2 or H/R. Data are presented as mean ± s.d. * $P<0.05$, ** $P<0.01$, n.s. $P>0.05$.

vivo investigations. First of all, the biosafety of HMOC-2 administration was comprehensively assessed using multiple methodologies. Hematoxylin and eosin staining of major organs revealed no histological toxicity following intravenous (i.v.) injection of HMOC-2 (**Figure S25**) into C57BL/6 mice. A pharmacokinetic and biodistribution study of HMOC-2 by i.v. injection was carried out above mice treated with renal I/R injury on left kidney. The distribution of Co and Ni within HMOC-2 was quantified by ICP-MS. The HMOC-2 has a significant enrichment effect in the left kidney (**Figure S26**). These findings were further corroborated by the blood biochemistry analysis results in mice treated with HMOC-2, demonstrating excellent tolerability at the administered dose (**Figure S27**). To evaluate the impact of HMOC-2 on renal I/R injury, all groups of mice were subjected to a 30-minute period of ischemia. Creatinine and blood urea nitrogen (BUN) levels were assessed at designated time points following reperfusion (Fig. 5**a-b**). The HMOC-2 treated group exhibited a significant decrease in serum levels compared to the I/R group, with peak values observed at 24 h post reperfusion (196.17 ± 24.29 versus 143 ± 24.61 for creatinine, and 69.67 ± 11.89 versus 50.5 ± 7.23 for BUN, respectively), then regressed progressively in subsequent periods. The histological evidence further supports the renal protective effect observed in HMOC-2 treated mice (Fig. 5**c-d**). The sham-operated mice, with or without HMOC-2 treatment, exhibited normal renal histology with no noticeable changes on morphology. Following reperfusion, kidneys from the HMOC-2 treated group showed minimal loss of brush border and limited intratubular debris or glomerular congestion, while the I/R group displayed more pronounced tubular necrosis. Two early kidney damage biomarkers, neutrophil gelatinase-associated lipocalin (NGAL) and kidney injury molecule-1 (KIM-1), were then evaluated among different groups using immunofluorescence (Fig. 5**e**). The results demonstrated a pronounced upregulation of NGAL and KIM-1 expression in I/R mice; however, treatment with HMOC-2 significantly attenuated this trend, particularly for NGAL, following renal reperfusion.

3.5. *HMOC-2 treatment attenuated I/R-induced inflammatory milieu*

Given its capacity to modulate inflammatory responses, oxidative stress emerges as a prominent determinant influencing renal injury. We

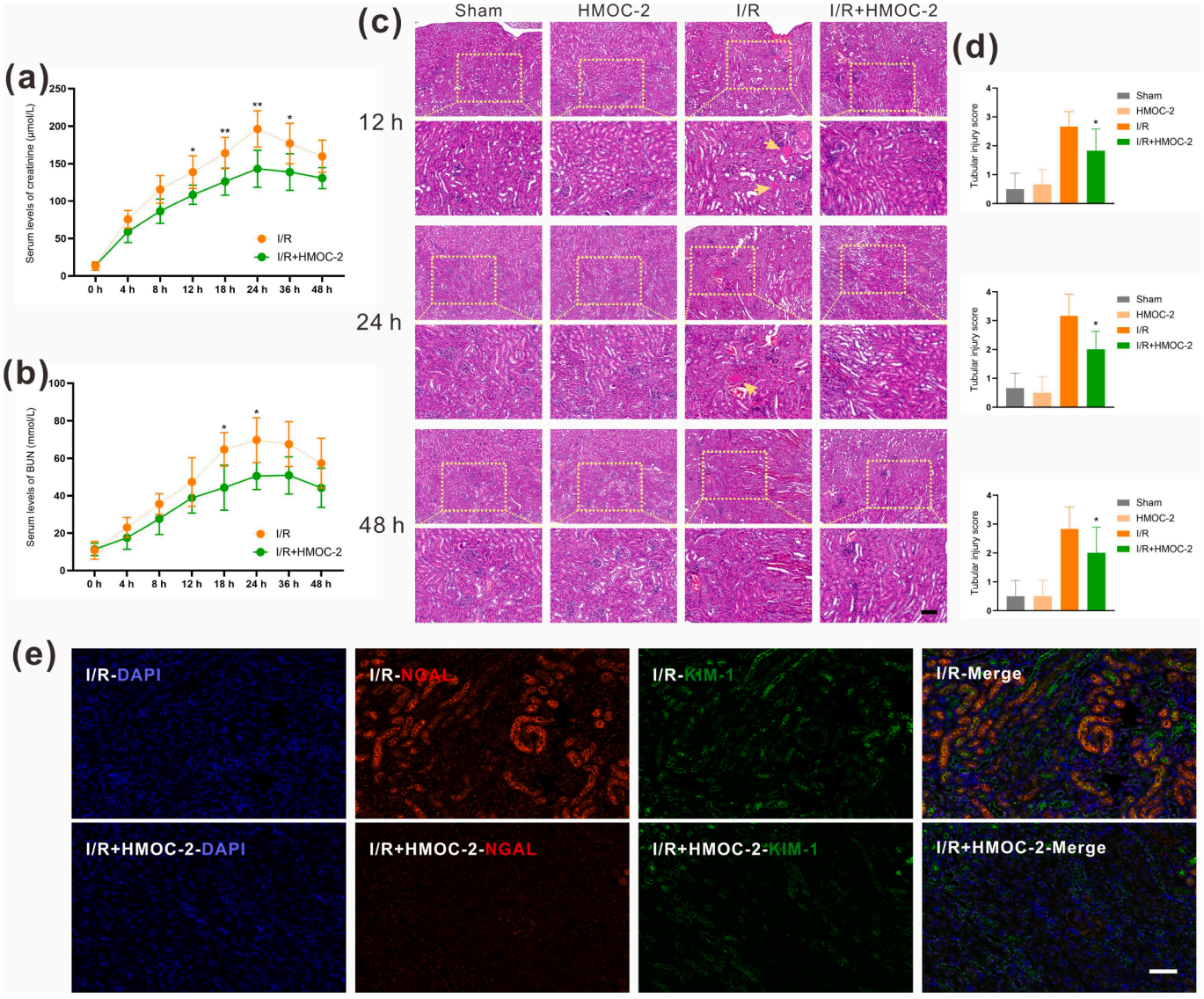

Fig. 5. HMOC-2 protected against renal I/R injury. (a-b) Serum creatinine and BUN levels in renal I/R injury. (c) Representative Hematoxylin and eosin staining of the kidney at 12, 24, and 48 h post reperfusion. Vascular congestion is indicated by arrows. Scale bar represents 50 μm. (d) Assessment of kidney injury based on tubular injury scores. (e) Representative immunofluorescence images showing NGAL and KIM-1 expression at 24 h post reperfusion. Scale bars represent 50 μm. Data are presented as mean ± s.d. * $P<0.05$, ** $P<0.01$.

next verified whether the amelioration of oxidative stress constitutes the underlying mechanism through which HMOC-2 confers renal protection against I/R injury (Fig. 6**a**). By employing dihydroethidium (DHE), an intracellular superoxide indicator which can be oxidized by superoxide to generate a red fluorescent product, we found that the fluorescence intensity of DHE-stained kidney tissue was increased in the I/R group compared to corresponding control mice, which suggests a high level of ROS production. This increase was reduced by HMOC-2 treatment, demonstrating that HMOC-2 inhibited I/R-induced oxidative stress in the kidneys. Considering the crucial roles of cytokines, including TNF-α, IL-2, IL-6, and IL-10 in I/R-induced renal injury, we compared their expression levels between HMOC-2-treated mice and control mice (Fig. 6**b**). Notably, mRNA levels for TNF-α, IL-2, and IL-6 were significantly lower in HMOC-2-treated mice than those in control mice. Conversely, the level of IL-10 exhibited a significant elevation in HMOC-2-treated mice as opposed to that observed in control mice. To elucidate the role of HMOC-2 in regulating neutrophil and macrophage infiltration following reperfusion, tissue samples were assessed using fluorescence immunostaining (with positive cells indicated by red fluorescence normalized to DAPI-stained nuclei). The areas exhibiting MPO positivity and CD68 expression represented neutrophil and macrophage infiltration, respectively (Fig. 6**c-f**). In comparison to the sham group, a significant augmentation in neutrophil and macrophage infiltration was observed in mice subjected to renal I/R injury; however, treatment with

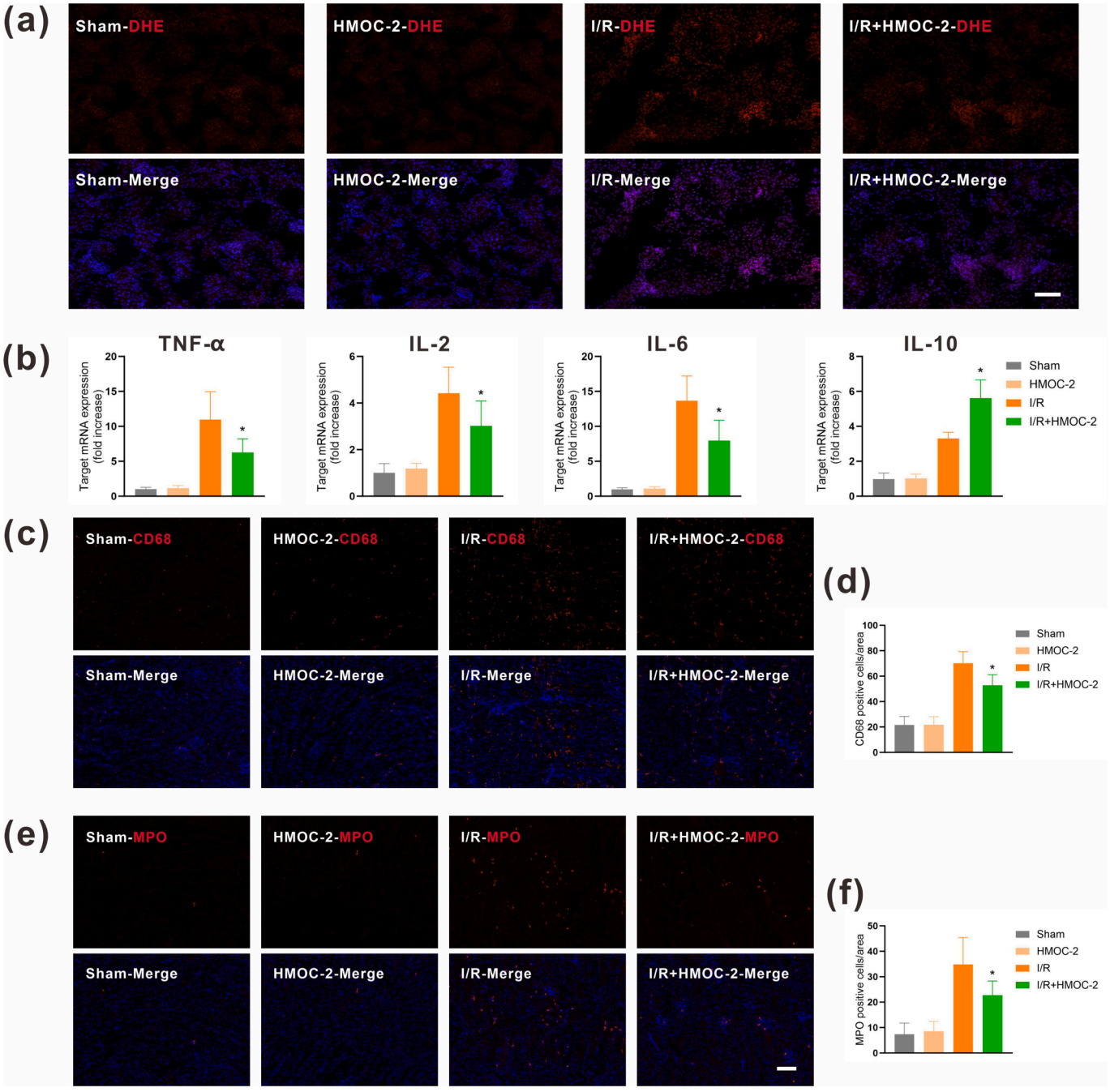

Fig. 6. In vivo renoprotective effects of HMOC-2 through its antioxidative and anti-inflammatory properties. (a) Representative immunofluorescence images of DHE expression at 24 h post reperfusion. Scale bar represents 50 μm. (b) The mRNA levels of TNF-α, IL-2, IL-6, and IL-10 in renal tissue. (c-d) Representative immunofluorescence images and the count of the CD68-positive cells. (e-f) Representative immunofluorescence images and the count of the MPO-positive cells. Scale bar represents 50 μm. Data are presented as mean ± s.d. * $P<0.05$.

HMOC-2 effectively mitigated this propensity.

3.6. HMOC-2 regulated I/R induced programmed cell death

Cell death is of equal importance to cell proliferation in the development and homeostasis of organ tissues. Programmed cell death (PCD), as a pivotal component of cell death, plays an indispensable role in maintaining cellular and tissue homeostasis under stress conditions. Pyroptosis, autophagy, and apoptosis represent the three pivotal forms of PCD, all of which are elicited in response to I/R injury. Pyroptosis is an inflammatory form of PCD that characterized by the activation of inflammatory caspase cysteine-dependent aspartate proteases and the release of IL-1β. To investigate whether the protective effect of HMOC-2 against renal I/R injury is through inhibiting NLRP3 inflammasome activation and subsequent pyroptosis, we utilized immunohistochemical (IHC) staining to assess the expression levels of IL-1β, caspase-1, NEK-7, and NLRP3 (Fig. 7**a**). The results demonstrated a significant increase in the number of IL-1β-positive cells following I/R injury, which was effectively attenuated by HMOC-2 treatment. Consistent findings were observed for caspase-1, NEK-7, and NLRP3 IHC results. To further validate these observations, we performed western blot analysis to assess the NLRP3 signaling pathway (Fig. 7**b**). In line with the IHC data, expression levels of NLRP3, pro-caspase-1, cleaved-caspase-1, and mature IL-1β were prominently upregulated after I/R injury; however, their quantification revealed a substantial reduction upon HMOC-2 intervention.

Because oxidative stress has been copiously reported as early inducers of autophagy upon nutrient deprivation, we next asked whether HMOC-2 would downregulate the level of autophagic flux, which may further exacerbate kidney damage in I/R injury by promoting

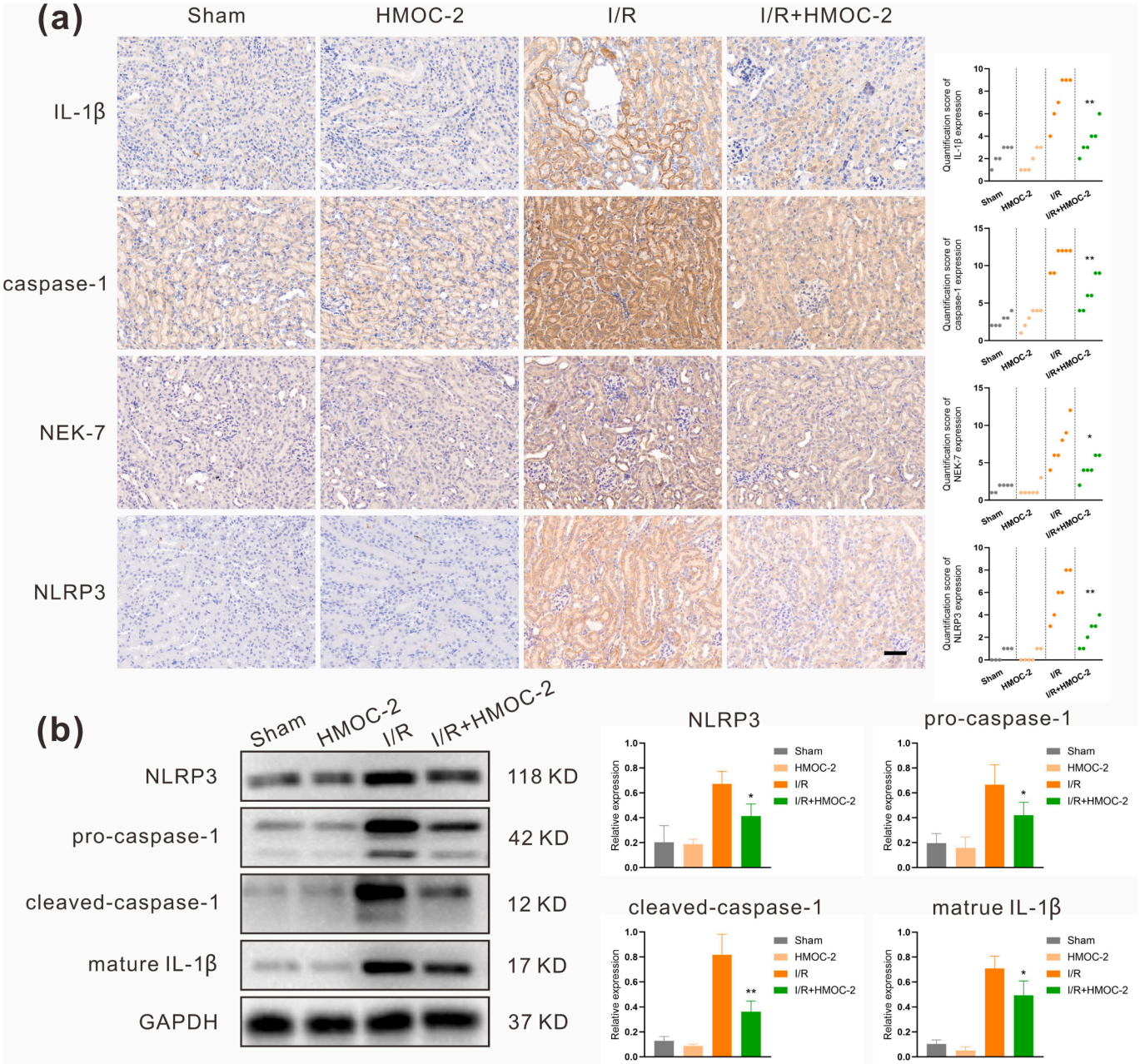

Fig. 7. HMOC-2 treatment reduced NLRP3-related pyroptosis during I/R injury. (a) Immunohistochemical staining and the count of IL-1β, caspase-1, NEK-7, and NLRP3. Scale bar represents 50 μm. (b) Expression of NLRP3, pro-caspase-1, cleaved-caspase-1, and mature-1β detected by western blotting assay. Data are presented as mean ± s.d. * $P<0.05$, ** $P<0.01$.

unnecessary degradation of cellular components, including proteins and organelles. The fluorescence immunostaining technique revealed a significant reduction in the number of LC3-positive cells following I/R insult after HMOC-2 treatment (LC3-positive cells indicated by red fluorescence normalized to DAPI-stained nuclei) (Fig. 8**a-b**). To validate these findings, we further examined the ultrastructure of kidney tissues using transmission electron microscopy (TEM) (Fig. 8**c**). Compared to the basal level observed in sham control, an increased presence of autophagic vacuoles was evident in the kidney tissues of I/R insulted mice; however, HMOC-2 treatment effectively attenuated this trend.

Apoptosis is a normal and essential process that occurs in all living organisms, as it helps to remove damaged or infected cells from the body. However, in certain situations, such as during disease progression or stressful conditions, the process can be exacerbated, leading to excessive cell death and tissue damage. The level of cellular apoptosis in I/R kidney was assessed using the TUNEL assay in this study (Fig. 8**d**). Our findings demonstrated that the percentages of TUNEL-positive cells were significantly lower in HMOC-2-treated groups compared to the control group. Specifically, the percentages of TUNEL-positive cells as a proportion of total renal cells were 0.98 % ± 0.66 %, 1.1 % ± 0.66 %, 10.27 % ± 3.52 %, and 6.1 % ± 1.77 % for the four respective groups, indicating a significant reduction in renal apoptosis following HMOC-2

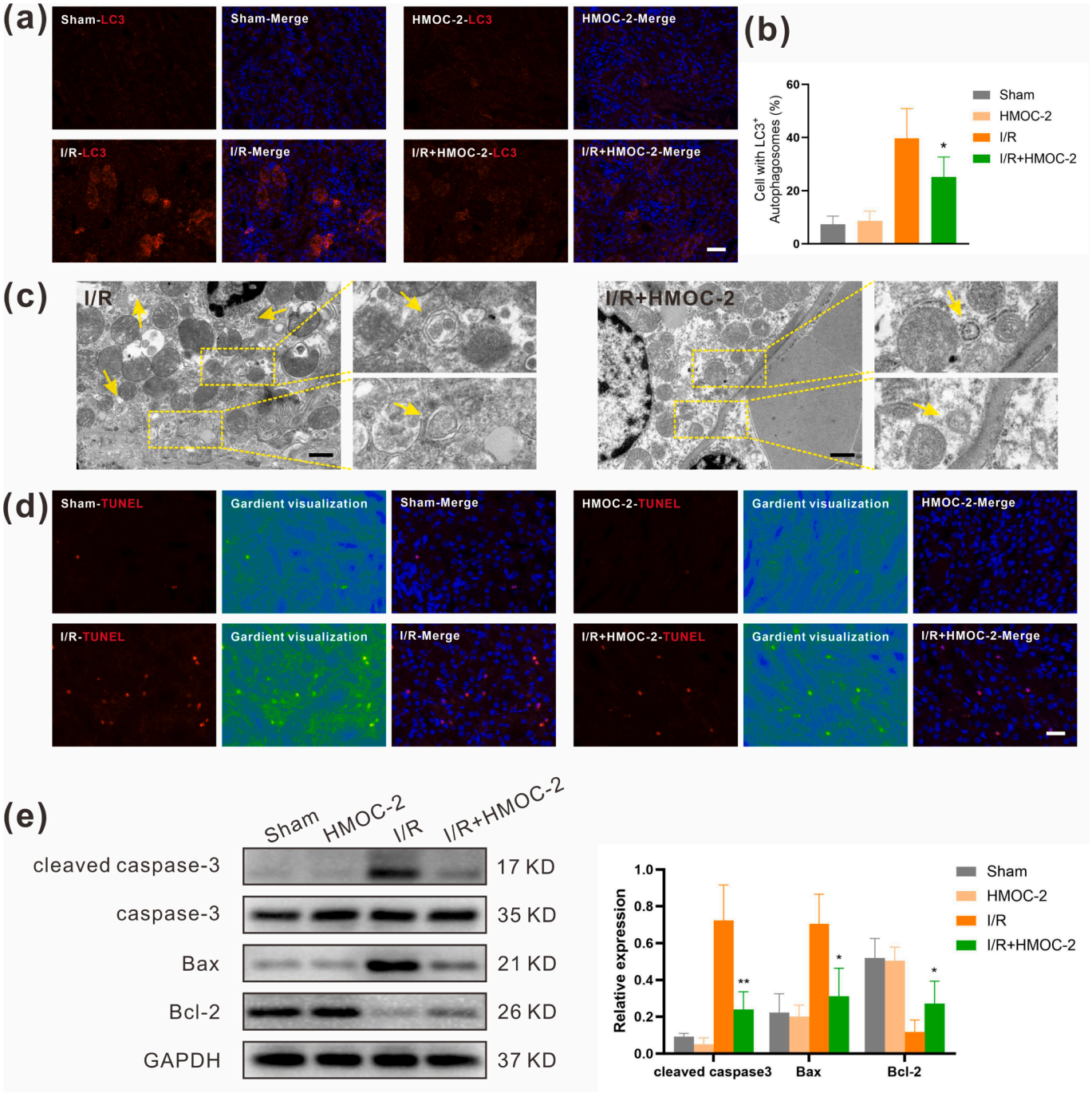

Fig. 8. HMOC-2 treatment downregulated the levels of autophagy and apoptosis in the kidney after I/R. (a-b) Representative immunofluorescence images and the percent of cell with LC3-positive autophagosomes. Scale bars represent 50 μm. (c) Ultrastructural changes in renal cells. Arrowheads indicate autophagic vesicles. Scale bars represent 1 μm. (d) Representative immunofluorescence of TUNEL-stained kidney sections. Scale bars represent 25 μm. (e) Expression of cleaved caspase-3, Bax, and Bcl-2 detected by western blotting assay. Data are presented as mean ± s.d. * $P<0.05$, ** $P<0.01$.

treatment. Given that caspase-cascade system, particularly caspase-3, plays a crucial role in apoptosis, we subsequently evaluated the expression levels of cleaved caspase-3, Bax, and Bcl-2 after kidney I/R injury through western blotting analysis (Fig. 8**e**). As anticipated, HMOC-2 treatment markedly decreased the expression levels of cleaved caspase-3 and pro-apoptotic protein Bax while increasing the level of anti-apoptotic protein Bcl-2.

4. Conclusion

In summary, in light of the challenges faced by existing nanozymes, such as imprecise structures or compositions, monotonous enzyme-like activities, and potential biosafety risks, we have developed MOC-based nanozymes featuring precise structures and multiple enzyme-like activities for the study of structure–function, controlled large-scale production, and further clinical translation. To this end, different metals were successfully incorporated into calixarene-based MOCs in a simple and controllable manner, thereby expanding the types and properties of MOCs. The obtained HMOCs with relatively well-defined structures can act as cascade antioxidant nanozymes with synergistically enhanced SOD-like and CAT-like activities. Moreover, the catalytic performance of the nanozymes can be finely tuned by manipulating the ratio between Co and Ni within HMOCs. The synergistic enhancement of antioxidant performance comes from the synergistic effect between two metals within a cluster verified through experimental results and theoretical calculations. The HMOC-based cascade nanozyme can effectively alleviate the renal I/R injury. The heterometallic organic cage-based nanozymes presents a promising avenue for advancing current research on artificial nanozymes with well-defined structures and multi enzyme-like activities, promoting the structure–activity interpretation and clinical translation. The strategy combing multiple metals also provides an effective method to introduce more types of metals into MOC on demand, thereby meeting the needs of different application scenarios, especially in the fields of biomedicine, energy, and environment. Regarding the structural precision of multi-metallic MOCs, metallic ligands and/or heterometallic clusters would be more effective strategies. Additionally, the incorporation of bioactive ligands, guests, and/or surfaces into MOCs can further broaden the properties and applications of MOCs. Post-synthetic modification is also a versatile strategy for the functionalization of MOCs.

CRediT authorship contribution statement

Demei Sun: Writing – original draft, Investigation. **Yucen Deng:** Investigation. **Jiayong Dong:** Investigation. **Xinyuan Zhu:** Resources. **Jinghui Yang:** Writing – review & editing, Supervision. **Youfu Wang:** Writing – review & editing, Supervision.

Declaration of competing interest

The authors declare that they have no known competing financial interests or personal relationships that could have appeared to influence the work reported in this paper.

Data availability

Data will be made available on request.

Acknowledgements

This work was supported by the National Key R&D Program of China (Key Special Project for Marine Environmental Security and Sustainable Development of Coral Reefs 2022-3.5), the Fundamental Research Funds for the Central Universities (YG2023QNA04, YG2022QN027), and Shanghai Municipal Health Commission Clinical Research Project (20214Y0521).

Appendix A. Supplementary material

Supplementary data to this article can be found online at https://doi.org/10.1016/j.cej.2024.154648.

References

[1] H.K. Eltzschig, T. Eckle, Ischemia and reperfusion—from mechanism to translation, Nat. Med. 17 (11) (2011) 1391–1401, https://doi.org/10.1038/nm.2507.
[2] G. Heusch, Myocardial ischaemia–reperfusion injury and cardioprotection in perspective, Nat. Rev. Cardiol. 17 (12) (2020) 773–789, https://doi.org/10.1038/s41569-020-0403-y.
[3] M. Zhang, Q. Liu, H. Meng, H. Duan, X. Liu, J. Wu, F. Gao, S. Wang, R. Tan, J. Yuan, Ischemia-reperfusion injury: molecular mechanisms and therapeutic targets, Signal Transduct. Target. Ther. 9 (1) (2024) 12, https://doi.org/10.1038/s41392-023-01688-x.
[4] S.F. Smith, S.A. Hosgood, M.L. Nicholson, Ischemia-reperfusion injury in renal transplantation: 3 key signaling pathways in tubular epithelial cells, Kidney Int. 95 (1) (2019) 50–56, https://doi.org/10.1016/j.kint.2018.10.009.
[5] N. Shiva, N. Sharma, Y.A. Kulkarni, S.R. Mulay, A.B. Gaikwad, Renal ischemia/reperfusion injury: an insight on in vitro and in vivo models, Life Sci. 256 (2020) 117860, https://doi.org/10.1016/j.lfs.2020.117860.
[6] J. Yang, H. Liu, S. Han, Z. Fu, J. Wang, Y. Chen, L. Wang, Melatonin pretreatment alleviates renal ischemia-reperfusion injury by promoting autophagic flux via TLR4/MyD88/MEK/ERK/mTORC1 signaling, FASEB J. 34 (9) (2020) 12324–12337, https://doi.org/10.1096/fj.202001252R.
[7] C. Ponticelli, F. Reggiani, G. Moroni, Delayed graft function in kidney transplant: risk factors, consequences and prevention strategies, J. Pers. Med. 12 (10) (2022) 1557, https://doi.org/10.3390/jpm12101557.
[8] L. Boutonnet, J. Mallard, A.-L. Charles, E. Hucteau, B. Gény, A. Lejay, A. Grandperrin, Autologous mitochondrial transplantation in male mice as a strategy to prevent deleterious effects of peripheral ischemia-reperfusion, Am. J. Physiol.: Cell Physiol. 326(2) (2024) 449-456. https://doi.org/10.1152/ajpcell.00639.2023.
[9] Y. Chen, Z. Li, H. Zhang, H. Chen, J. Hao, H. Liu, X. Li, Mitochondrial metabolism and targeted treatment strategies in ischemic-induced acute kidney injury, Cell Death Discov. 10 (1) (2024) 69, https://doi.org/10.1038/s41420-024-01843-5.
[10] I. Tyuryaeva, O. Lyublinskaya, Expected and unexpected effects of pharmacological antioxidants, Int. J. Mol. Sci. 24 (11) (2023) 9303, https://doi.org/10.3390/ijms24119303.
[11] H.N. Geo, D.D. Murugan, Z. Chik, A. Norazit, Y.Y. Foo, B.F. Leo, Y.Y. Teo, S.Z.S.B.S. A. Kadir, Y. Chan, H.J. Chai, M. Medel, N.A. Abdullah, E.J. Johns, M.J. Vicent, L. Y. Chung, L.V. Kiew, Renal nano-drug delivery for acute kidney injury: current status and future perspectives, J. Controlled Release 343 (2022) 237–254, https://doi.org/10.1016/j.jconrel.2022.01.033.
[12] C. Ding, B. Wang, J. Zheng, M. Zhang, Y. Li, H.-H. Shen, Y. Guo, B. Zheng, P. Tian, X. Ding, W. Xue, Neutrophil membrane-inspired nanorobots act as antioxidants ameliorate ischemia reperfusion-induced acute kidney injury, ACS Appl. Mater. Interfaces 15 (34) (2023) 40292–40303, https://doi.org/10.1021/acsami.3c08573.
[13] Y. Zhang, W. Gao, Y. Ma, L. Cheng, L. Zhang, Q. Liu, J. Chen, Y. Zhao, K. Tu, M. Zhang, C. Liu, Integrating Pt nanoparticles with carbon nanodots to achieve robust cascade superoxide dismutase-catalase nanozyme for antioxidant therapy, Nano Today 49 (2023) 101768, https://doi.org/10.1016/j.nantod.2023.101768.
[14] Q. Chen, Y. Nan, Y. Yang, Z. Xiao, M. Liu, J. Huang, Y. Xiang, X. Long, T. Zhao, X. Wang, Q. Huang, K. Ai, Nanodrugs alleviate acute kidney injury: manipulate RONS at kidney, Bioact. Mater. 22 (2023) 141–167, https://doi.org/10.1016/j.bioactmat.2022.09.021.
[15] Y. Dai, Y. Ding, L. Li, Nanozymes for regulation of reactive oxygen species and disease therapy, Chin. Chem. Lett. 32 (9) (2021) 2715–2728, https://doi.org/10.1016/j.cclet.2021.03.036.
[16] M. Liang, X. Yan, Nanozymes: from new concepts, mechanisms, and standards to applications, Acc. Chem. Res. 52 (8) (2019) 2190–2200, https://doi.org/10.1021/acs.accounts.9b00140.
[17] J. Wu, X. Wang, Q. Wang, Z. Lou, S. Li, Y. Zhu, L. Qin, H. Wei, Nanomaterials with enzyme-like characteristics (nanozymes): next-generation artificial enzymes (II), Chem. Soc. Rev. 48 (4) (2019) 1004–1076, https://doi.org/10.1039/C8CS00457A.
[18] Z. Guo, J. Hong, N. Song, M. Liang, Single-atom nanozymes: from precisely engineering to extensive applications, Acc. Mater. Res. 5 (3) (2024) 347–357, https://doi.org/10.1021/accountsmr.3c00250.
[19] Y. Huang, J. Ren, X. Qu, Nanozymes: classification, catalytic mechanisms, activity regulation, and applications, Chem. Rev. 119 (6) (2019) 4357–4412, https://doi.org/10.1021/acs.chemrev.8b00672.
[20] W. Yang, X. Yang, L. Zhu, H. Chu, X. Li, W. Xu, Nanozymes: activity origin, catalytic mechanism, and biological application, Coord. Chem. Rev. 448 (2021) 214170, https://doi.org/10.1016/j.ccr.2021.214170.
[21] C. Cao, N. Yang, X. Wang, J. Shao, X. Song, C. Liang, W. Wang, X. Dong, Biomedicine meets nanozyme catalytic chemistry, Coord. Chem. Rev. 491 (2023) 215245, https://doi.org/10.1016/j.ccr.2023.215245.
[22] M. Zandieh, J. Liu, Nanozymes: definition, activity, and mechanisms, Adv. Mater. 36 (2024) 2211041, https://doi.org/10.1002/adma.202211041.
[23] D. Jiang, D. Ni, Z.T. Rosenkrans, P. Huang, X. Yan, W. Cai, Nanozyme: new horizons for responsive biomedical applications, Chem. Soc. Rev. 48 (14) (2019) 3683–3704, https://doi.org/10.1039/C8CS00718G.

[24] Z. Wang, R. Zhang, X. Yan, K. Fan, Structure and activity of nanozymes: Inspirations for de novo design of nanozymes, Mater. Today 41 (2020) 81–119, https://doi.org/10.1016/j.mattod.2020.08.020.
[25] M. Wei, J. Lee, F. Xia, P. Lin, X. Hu, F. Li, D. Ling, Chemical design of nanozymes for biomedical applications, Acta Biomater. 126 (2021) 15–30, https://doi.org/10.1016/j.actbio.2021.02.036.
[26] Y. Ai, Z.-N. Hu, X. Liang, H. Sun, H. Xin, Q. Liang, Recent advances in nanozymes: from matters to bioapplications, Adv. Funct. Mater. 32 (14) (2022) 2110432, https://doi.org/10.1002/adfm.202110432.
[27] F. Attar, M.G. Shahpar, B. Rasti, M. Sharifi, A.A. Saboury, S.M. Rezayat, M. Falahati, Nanozymes with intrinsic peroxidase-like activities, J. Mol. Liq. 278 (2019) 130–144, https://doi.org/10.1016/j.molliq.2018.12.011.
[28] E.M. Hamed, V. Rai, S.F.Y. Li, Single-atom nanozymes with peroxidase-like activity: a review, Chemosphere 346 (2024) 140557, https://doi.org/10.1016/j.chemosphere.2023.140557.
[29] H. Zhao, R. Zhang, X. Yan, K. Fan, Superoxide dismutase nanozymes: an emerging star for anti-oxidation, J. Mater. Chem. B 9 (35) (2021) 6939–6957, https://doi.org/10.1039/D1TB00720C.
[30] D. Xu, L. Wu, H. Yao, L. Zhao, Catalase-like nanozymes: classification, catalytic mechanisms, and their applications, Small 18 (37) (2022), https://doi.org/10.1002/smll.202203400.
[31] S. Zhou, H. Cai, X. He, Z. Tang, S. Lu, Enzyme-mimetic antioxidant nanomaterials for ROS scavenging: design, classification, and biological applications, Coord. Chem. Rev. 500 (2024) 215536, https://doi.org/10.1016/j.ccr.2023.215536.
[32] N.T.M. Thao, H.D.K. Do, N.N. Nam, N.K.S. Tran, T.T. Dan, K.T.L. Trinh, Antioxidant nanozymes: mechanisms, activity manipulation, and applications, Micromachines 14 (5) (2023) 1017, https://doi.org/10.3390/mi14051017.
[33] X. Liu, H. Xu, H. Peng, L. Wan, D. Di, Z. Qin, L. He, J. Lu, S. Wang, Q. Zhao, Advances in antioxidant nanozymes for biomedical applications, Coord. Chem. Rev. 502 (2024) 215610, https://doi.org/10.1016/j.ccr.2023.215610.
[34] L. Su, S. Qin, Z. Xie, L. Wang, K. Khan, A.K. Tareen, D. Li, H. Zhang, Multi-enzyme activity nanozymes for biosensing and disease treatment, Coord. Chem. Rev. 473 (2022) 214784, https://doi.org/10.1016/j.ccr.2022.214784.
[35] J. Sheng, Y. Wu, H. Ding, K. Feng, Y. Shen, Y. Zhang, N. Gu, Multienzyme-like nanozymes: regulation, rational design, and application, Adv. Mater. 36 (10) (2024) 2211210, https://doi.org/10.1002/adma.202211210.
[36] S. Lee, H. Jeong, D. Nam, M.S. Lah, W. Choe, The rise of metal–organic polyhedra, Chem. Soc. Rev. 50 (1) (2021) 528–555, https://doi.org/10.1039/D0CS00443J.
[37] C.T. McTernan, J.A. Davies, J.R. Nitschke, Beyond platonic: how to build metal–organic polyhedra capable of binding low-symmetry, information-rich molecular cargoes, Chem. Rev. 122 (11) (2022) 10393–10437, https://doi.org/10.1021/acs.chemrev.1c00763.
[38] J. Liu, Z. Wang, P. Cheng, M.J. Zaworotko, Y. Chen, Z. Zhang, Post-synthetic modifications of metal–organic cages, Nat. Rev. Chem. 6 (5) (2022) 339–356, https://doi.org/10.1038/s41570-022-00380-y.
[39] Y. Wang, Y. Zhang, X. Duan, J.-J. Mao, M. Pan, J. Shen, C. Su, Recent progress in metal-organic cages for biomedical application: Highlighted research during 2018–2023, Coord. Chem. Rev. 501 (2024) 215570, https://doi.org/10.1016/j.ccr.2023.215570.
[40] D. Sun, X. Feng, X. Zhu, Y. Wang, J. Yang, Anticancer agents based on metal organic cages, Coord. Chem. Rev. 500 (2024) 215546, https://doi.org/10.1016/j.ccr.2023.215546.
[41] C. Huang, Y. Deng, R. Ma, H. Ge, F. Gong, J. Yang, X. Zhu, Y. Wang, A metal-organic cage-derived cascade antioxidant nanozyme to mitigate renal ischemia-reperfusion injury, Nanoscale 16 (19) (2024) 9406–9411, https://doi.org/10.1039/d4nr00742e.
[42] X. Ning, P. Yin, L. Zhang, F. Gao, Y. Wang, J. Yang, A biocompatible Mn-decorated metal–organic cage with sustainable CO release, New J. Chem. 48 (15) (2024) 6557–6561, https://doi.org/10.1039/d3nj05363f.
[43] L.K. Moree, L.A.V. Faulkner, J.D. Crowley, Heterometallic cages: synthesis and applications, Chem. Soc. Rev. 53 (1) (2024) 25–46, https://doi.org/10.1039/D3CS00690E.
[44] F. Li, L.F. Lindoy, Complementarity and preorganisation in the assembly of heterometallic–organic cages via the metalloligand approach—recent advances, Chemistry 4 (4) (2022) 1439–1456, https://doi.org/10.3390/chemistry4040095.
[45] Y. Liu, Y. Cheng, H. Zhang, M. Zhou, Y. Yu, S. Lin, B. Jiang, X. Zhao, L. Miao, C.-W. Wei, Q. Liu, Y. Lin, Y. Du, C.J. Butch, H. Wei, Integrated cascade nanozyme catalyzes in vivo ROS scavenging for anti-inflammatory therapy, Sci. Adv. 6 (29) (2020), https://doi.org/10.1126/sciadv.abb2695.
[46] X. Cai, L. Jiao, H. Yan, Y. Wu, W. Gu, D. Du, Y. Lin, C. Zhu, Nanozyme-involved biomimetic cascade catalysis for biomedical applications, Mater. Today 44 (2021) 211–228, https://doi.org/10.1016/j.mattod.2020.12.005.
[47] X. Zhang, G. Li, G. Chen, D. Wu, Y. Wu, T.D. James, Enzyme mimics for engineered biomimetic cascade nanoreactors: mechanism, applications, and prospects, Adv. Funct. Mater. 31 (50) (2021), https://doi.org/10.1002/adfm.202106139.
[48] P. Buchwalter, J. Rosé, P. Braunstein, Multimetallic catalysis based on heterometallic complexes and clusters, Chem. Rev. 115 (1) (2015) 28–126, https://doi.org/10.1021/cr500208k.
[49] S. Li, A. Wang, P. Yuan, L. Mei, L. Zhang, J. Feng, Heterometallic nanomaterials: activity modulation, sensing, imaging and therapy, Chem. Sci. 13 (19) (2022) 5505–5530, https://doi.org/10.1039/D2SC00460G.
[50] M.R. Dworzak, M.M. Deegan, G.P.A. Yap, E.D. Bloch, Synthesis and characterization of an isoreticular family of calixarene-capped porous coordination cages, Inorg. Chem. 60 (8) (2021) 5607–5616, https://doi.org/10.1021/acs.inorgchem.0c03554.
[51] K.-K. Liu, Z.-J. Guan, M. Ke, Y. Fang, Bridging the gap between charge storage site and transportation pathway in molecular-cage-based flexible electrodes, ACS Cent. Sci. 9 (4) (2023) 805–815, https://doi.org/10.1021/acscentsci.3c00027.
[52] Q. Liu, H. Cong, H. Deng, Deciphering the spatial arrangement of metals and correlation to reactivity in multivariate metal–organic frameworks, J. Am. Chem. Soc. 138 (42) (2016) 13822–13825, https://doi.org/10.1021/jacs.6b08724.
[53] Y. Liang, Y. Fang, Y. Cui, H. Zhou, A stable biocompatible porous coordination cage promotes in vivo liver tumor inhibition, Nano Res. 14 (10) (2021) 3407–3415, https://doi.org/10.1007/s12274-021-3646-y.
[54] L. Chen, J. Duan, P. Du, W. Sun, B. Lai, W. Liu, Accurate identification of radicals by in-situ electron paramagnetic resonance in ultraviolet-based homogenous advanced oxidation processes, Water Res. 221 (2022) 118747. https://doi.org/10.1016/j.watres.2022.118747.
[55] P. Huang, P. Zhang, C. Wang, J. Tang, H. Sun, Enhancement of persulfate activation by Fe-biochar composites: synergism of Fe and N-doped biochar, Appl. Catal. B: Environ. 303 (2022) 120926. https://doi.org/10.1016/j.apcatb.2021.120926.
[56] G. Xu, K. Liu, B. Jia, Z. Dong, C. Zhang, X. Liu, Y. Qu, W. Li, M. Zhao, H. Zhou, Y.-Q. Li, Electron lock manipulates the catalytic selectivity of nanozyme, ACS Nano 18 (4) (2024) 3814–3825, https://doi.org/10.1021/acsnano.3c12201.
[57] Z. Wang, J. Wu, J.-J. Zheng, X. Shen, L. Yan, H. Wei, X. Gao, Y. Zhao, Accelerated discovery of superoxide-dismutase nanozymes via high-throughput computational screening, Nat. Commun. 12 (1) (2021) 6866, https://doi.org/10.1038/s41467-021-27194-8.
[58] W. Gao, J. He, L. Chen, X. Meng, Y. Ma, L. Cheng, K. Tu, X. Gao, C. Liu, M. Zhang, K. Fan, D. Pang, X. Yan, Deciphering the catalytic mechanism of superoxide dismutase activity of carbon dot nanozyme, Nat. Commun. 14 (1) (2023) 160, https://doi.org/10.1038/s41467-023-35828-2.
[59] A. Aranda, L. Sequedo, L. Tolosa, G. Quintas, E. Burello, J.V. Castell, L. Gombau, Dichloro-dihydro-fluorescein diacetate (DCFH-DA) assay: a quantitative method for oxidative stress assessment of nanoparticle-treated cells, Toxicol. in Vitro 27 (2) (2013) 954–963, https://doi.org/10.1016/j.tiv.2013.01.016.